

Magnetic, electronic and vibrational properties of metal and fluorinated metal phthalocyanines

O. I. Arillo-Flores¹, M. M. Fadlallah^{2,3}, C. Schuster², U. Eckern², and A. H. Romero^{1,4,5*}

¹*CINVESTAV-Querétaro Libramiento Norponiente No.*

2000 Real de Juriquilla 76230 Querétaro, Qro, México

²*Institut für Physik, Universität Augsburg, 86135 Augsburg, Germany*

³*Physics Department, Faculty of Science, Benha University, Benha, Egypt*

⁴*Max-Planck-Institute für Mikrostrukturphysik,*

Weinberg 2, 06120 Halle, Germany

⁵*Physics Department, West Virginia University,*

Morgantown, West Virginia 26506-6315, USA

(Dated: February 6, 2013)

Abstract

The magnetic and electronic properties of metal phthalocyanines (MPc) and fluorinated metal phthalocyanines (F₁₆MPc) are studied by means of spin density functional theory (SDFT). Several metals (M) such as Ca, all first *d*-row transition metals and Ag are investigated. By considering different open shell transition metals it is possible to tune the electronic properties of MPc, in particular the electronic molecular gap and total magnetic moment. Besides assigning the structural and electronic properties of MPc and F₁₆MPc, the vibrational modes analysis of the ScPc–ZnPc series have been studied and correlated to experimental measurements when available.

PACS numbers: 31.15.ae, 75.50.Xx

Keywords: Density functional theory, magnetic moments, phthalocyanine

* aromero@qro.cinvestav.mx

I. INTRODUCTION

Magnetism or magnetic moments are rarely found in organic compounds, but metal phthalocyanine (MPc) molecules are notable exceptions [1]. The MPc family represents metal-organic semiconductors that display high thermal and chemical stability [2]. These molecules have recently attracted large interest in applications such as in solar cells, optoelectronic devices, light-emitting diodes, thin-film transistors, and gas sensors [3–7]. The magnetic properties of CoPc are used in spintronic devices [8]. Furthermore, the MPc are simple magnetic molecules which can serve as prototypical systems to study the magnetic properties of the $3d$ transition metals embedded in an organic surrounding.

Fluorinated metal-phthalocyanines (F_{16} MPc) are also widely used in applications. In contrast to the MPc which usually are p-type like semiconductors, F_{16} MPc are used as n-type semiconductors in photovoltaic devices and in light-emitting diodes. Organic field-effect transistors have been intensively studied as components for low price, large area, and flexible circuit applications. To build them, an n-type organic semiconductor is needed. Experimental investigations focus on F_{16} CuPc [9, 10] and F_{16} CoPc [11–14]. They have been also considered as an alternative to inorganic field-effect transistors (FETs) in some specific circuit applications such as radio frequency identification cards (RFIDs) [15, 16], electronic paper [17], sensors [18, 19], and switching devices for active matrix flat panel displays (AMFPDs) [20].

Several experimental techniques as X-ray spectroscopy [21–25], neutron diffraction [21–25], scanning tunneling microscopy (STM) [26, 27], nuclear magnetic resonance [28], and photo-emission spectroscopy [29] have been used to characterize the structural and electronic properties of MPc. However, for further developments in the synthesis and production of novel materials and devices based on MPc, more accessible and common techniques such as IR and Raman spectroscopy are useful. For example, Raman scattering has already been employed to identify different metal phthalocyanines and to probe polymorphic changes (packing) [30], as well as structural modifications [31]. Therefore, a systematic study of vibrational modes for the series MPc will provide information on the resolution of spectral features obtained with ultraviolet photo-electron, x-ray photo-emission and photoabsorption spectroscopy measurements. Vibrational coupling effects have been found to have an important effect in the description of outer molecular orbitals of CuPc [24], as well as of valence

bands and core levels of PbPc films [32]. The study of vibrational properties can help to improve the assessment of other theoretical methods used to study metal-organic complexes [33], and to correlate magnetic transitions to changes of the surrounding [34].

From a theoretical point of view, density functional theory (DFT) is a widely used method to determine the electronic structure of various organic molecules, including MPc [31, 35, 36]. Bialek *et al.* applied an all-electron full-potential linearized augmented plane-wave method to study the electronic structure and magnetic moments of NiPc, CuPc, FePc, and CoPc [37–40]. Marom *et al.* have tested a variety of exchange correlation functionals for copper phthalocyanine [41], comparing local functionals such as LDA (local density approximation) [42] and GGA (generalized gradient approximation) [43, 44] with the semiempirical hybrid functional B3LYP [45], the non-empirical PBE [46], PBE hybrid (PBEh) [47], and the screened HSE [48]. While all these functionals describe the geometrical structure quite well, the local functionals underestimate the binding of orbitals at the molecule center. Additionally, GGA+U calculations have been performed in Ref. [49] to take into account the strong correlations that could be relevant around the metal center.

The present article is organized as follows. After a brief description of the computational method in Section II, we report in Section III our results for the magnetic and electronic structure of CaPc, of the sequence of 3*d* MPc ($M = \text{Sc, Ti, V, Cr, Mn, Fe, Co, Ni, Cu, Zn}$), and of 4*d* AgPc. In addition, we compare the electronic properties of the fluorinated MPc (F_{16}MPc) and MPc. In Section IV we present our results for the vibrational properties of MPc, and we analyze general trends. A brief summary is given in Section V.

II. COMPUTATIONAL METHODS

In the present work, we focus on studying the electronic structure near the Fermi energy, E_F , and the magnetic structure by means of density functional theory. Since hybrid functionals with a stronger amount of Fock exchange tend to overestimate magnetic moments and magnetic order, we apply the simplest exchange correlation functional, namely the LDA, as implemented in the SIESTA package [50]. The electronic structure and the vibrational modes are calculated in MPc and F_{16}MPc by using this implementation. The calculations have been performed by considering a finite spin polarization to allow for the formation of local magnetic moments. The PBE method [46] is also employed in order to compare with

the density of states (DOS) evaluated with LDA.

Wavefunctions in SIESTA are described by a local atomic orbitals basis set; we have used a double zeta basis set and an energy cutoff of 300 Ry. The pseudo potentials are norm-conserving in fully non-local form. Structural optimizations were performed using the conjugate gradient method until net force on every atom was smaller than 0.04 eV/Å. Non-symmetrical constraints were employed. At the optimized geometries, force constants were evaluated and employed to calculate vibrational modes and frequencies through the dynamical matrix. As we are interested in the electronic structure and vibrational properties of single molecules, we restrict our calculations to the Γ point, and a large simulation box of $28 \text{ Å} \times 27 \text{ Å} \times 45 \text{ Å}$ was used, to avoid periodic images interactions. Further geometry optimization and frequency calculations of selected systems were also carried out with B3LYP/6-31G** in the Gaussian 03 suit of packages, in order to identify, by comparison with previous results, the IR and Raman representations.

III. MAGNETIC AND ELECTRONIC PROPERTIES OF METAL PHTHALOCYANINE

Metal phthalocyanine, $\text{MC}_{32}\text{N}_8\text{H}_{16}$, is an aromatic molecule with the molecular structure shown in Fig. 1. Hexadecafluorophthalocyaninatometal, F_{16}MPc , is constructed by replacing the hydrogen atoms within MPc with fluor atoms. It is expected that the metal (M) is located at the center of the molecule, displaying a square planar symmetry D_{4h} [51]. The structural, electronic and magnetic properties of MPc are controlled by the particular characteristics of the metal within the inner ring. Phenyl groups contribute to the stabilization of these molecular complexes and influence their charge distribution, as reported for the formation of ScPc_2 [52, 53]. Nonetheless, they may be subject to oxidation as in the case of TiPc [53–55] and VPc [56, 57].

To study the magnetic structure of the first row transition metals and also of Ca and of Ag within an isolated MPc, we first focus on the determination of their geometrical structure, and on how our observations relate to our approximations and the different molecular components.

In general the optimized structures show a planar geometry except for the ScPc and CaPc , where the metal is slightly out-of-plane while the rest of the molecule undergoes a

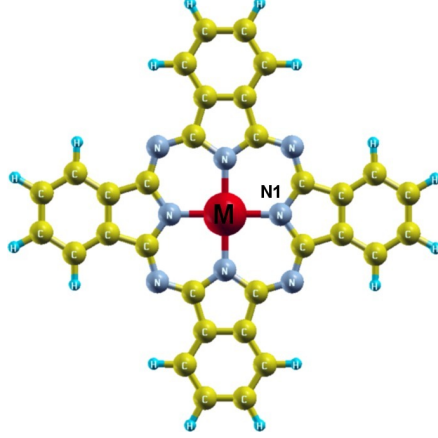


FIG. 1. (Color online) Structure under investigation: metal phthalocyanine (MPc) molecule. The atoms are labeled according to the chemical constituents, and the metal atom in the center is denoted by M.

small bending towards the opposite direction. This effect becomes larger as the atomic radius of the metal increases, the Sc atom (with radius of 1.62 Å) is displaced by 0.24 Å from the molecular plane while Ca (with radius of 1.97 Å) is shifted by 1.12 Å. To confirm the observed trend we calculate the optimized geometry for YPc obtaining an out-of-plane displacement of 0.72 Å. It can be seen from Fig. 2 that for ScPc the valence electron density (isosurface value = 0.15) appears distant from the metal center, beyond the Van der Waals radius of Sc, i.e., the metal departure from the molecular plane is caused by the repulsion between inner electron shells on the metal and on adjacent atoms. In the distorted geometry the metal is more exposed and the molecular liability increases.

Geometrical structures of minimal energy may be influenced by a Jahn-Teller distortion, which tends to reduce the symmetry from D_{4h} to D_{2h} . As the point group symmetry was not constrained through our geometry optimizations, strictly speaking we have obtained, for MPc planar geometries, the D_{2h} symmetry with two M-N distances slightly different from each other, nevertheless they differ only by less than 1 %, this variation being in order of magnitude comparable to the precision of the energy minimization procedure. A detailed account of the Jahn-Teller distortion effect on the studied MPc series is beyond the scope of the present work. Interested readers are referred to the work of Marom and Kronik [58] who emphasize the theoretical and experimental difficulties to describe precisely the electronic states of MnPc and FePc, the differences being due to their intricate potential energy surface.

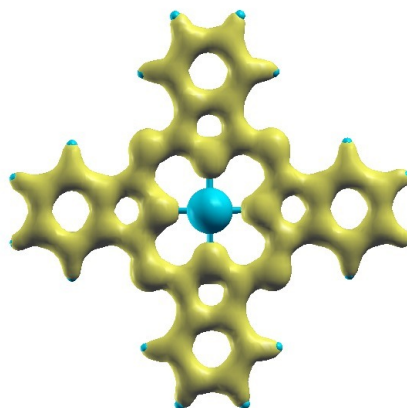


FIG. 2. (Color online) Charge density for ScPc. Isosurface value = 0.15

Table I shows the bond lengths between the metal and the nitrogen N1, as indicated in Fig. 1. When available, we compare to experimental data. The theoretical bond lengths differ from experimental lengths by less than 0.05 Å, i.e., by 1 to 2 %. Decreasing the atomic covalent radius leads to a decrease in the bond length from Sc to Cr, as well as from Mn to Cu. In F₁₆MPc, the M–N1 bond length is typically slightly larger than in MPc, as shown in Tab. I. The influence of the larger radius of fluorine with respect to hydrogen, and its *p* electrons show up only when no metallic states are present near the Fermi level.

The last row of Tab. I shows the magnetic moments of MPc (in the case of F₁₆MPc molecules, the calculated magnetic moments are quite close to the related MPc). Along the sequence from M = Sc to Mn, an open *d*-shell on the metal progressively becomes half-filled and the MPc magnetic moments closely follow the tendency on the metal center (Sc ($s = 1/2$, $3d^1$), Ti ($s = 1$, $3d^2$), V ($s = 3/2$, $3d^3$), Cr ($s = 2$, $3d^4$), and Mn ($s = 5/2$, $3d^5$)). The magnetic moment found for MnPc, $5\mu_B$, is larger than the previously reported value of $3\mu_B$ [59], however, high magnetic moments within this series are also obtained using PBE. In the second half of the *d*-shell, total spin values lie between 0 and 2. In general, they are smaller than those predicted for the first half. The values found for this interval agree very well with earlier results [2, 60, 61]. Therefore, the trend in the magnetic moment can be correlated with the electron pairing and the crystal field created by the molecule to the metallic atom, which reduces the covalent character. The atomic orbitals hybridize such that they originate a new mixing, altering the expected orbital ordering from the plain crystalline

field effect, when it goes only over the non-hybridized atomic orbitals. As a consequence there is an abrupt decrease of magnetic moment from Mn to Fe, and zero magnetic moments are found for NiPc before completing the d -shell. CuPc ($s = 1/2$, $3d^9$) and AgPc ($s = 1/2$, $4d^9$) have a hole in their nearly full d -shell. The fact that magnetic moments for F_{16} MPc are similar to those for MPc suggests that molecular magnetic moment are strongly influenced by contributions to the total electronic density coming from the metal center, with less dependence on the molecular environment; this observation holds for Ag and even Ca, an s -block element.

The observed tendency for M–N1 bond lengths results from two main factors. The first one is the metal atomic radius reduction along the period, which clearly dominates from Ca to V, and the second one is the increase of electronic repulsion for high spin values and degree of orbital occupancy; these effects overcome the first one for Cr. In the second half of the d -row, the decrease in magnetic moment values is reflected in the M–N1 bond lengths variation from Fe to Cu. Deviation from such behavior in the case of ZnPc may be understood by electron accumulation on the metal when the d -shell is full, and the resulting increase of electronic repulsion.

TABLE I. M–N1 bond lengths (Å) and magnetic moments (\mathbf{m} (μ_B)) for MPc and F_{16} MPc

M		Ca	Sc	Ti	V	Cr	Mn	Fe	Co	Ni	Cu	Zn	Ag
Bond	MPc	2.322	1.998	1.974	1.968	1.971	2.012	1.912 1.927 ^a	1.883 1.912 ^b	1.875 1.83 ^c	1.937 1.935 ^d	1.975 1.980 ^e 1.954 ^f	2.042
	F_{16} MPc	2.328	1.992	1.988	1.974	1.975	2.021	1.991	1.888	1.884	1.947	1.988	2.044
\mathbf{m}	MPc	0.00	0.99	2.00	3.00	4.00	4.80	2.00	1.00	0.00	1.00	0.00	0.95

^a, ^b, ^c, ^d, ^e and ^f from references [22], [62], [63], [21], [23] and [64], respectively.

To complement the analysis of the magnetic properties of the MPc, we discuss their spin resolved electronic structure in the following. Firstly, we consider the density of states (DOS) of CaPc and F_{16} CaPc shown in Fig. 3. Here and in the following plots, the density of states of one of the two spin components is multiplied by -1 . Additionally, a level broadening of molecular orbital energies with a spread of 0.1 eV is used to simulate thermal and anharmonic effects in the spectra. The energy is shifted with respect to the Fermi level E_F , estimated

using the Fermi-Dirac function with an electronic temperature of 300 K. The energy gap of CaPc, estimated as the difference between its highest occupied molecular orbital (HOMO) and its lowest unoccupied molecular orbital (LUMO), is 1.3 eV. As it can be noted in Fig. 3, these orbitals have no metal contribution, and they are localized upon the Pc atoms. Both peaks are very similar to the fluorinated derivative, the main difference is the decrease of the energy gap by 0.2 eV. However, the shape of the HOMO-1 (first orbital with an energy below the HOMO energy), is quite different: it is very broad in F₁₆CaPc, in contrast to CaPc where it is rather narrow, indicating several energy states close by.

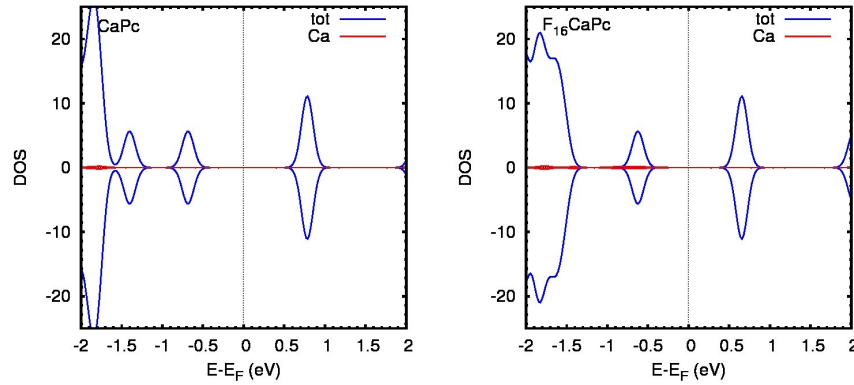


FIG. 3. (Color online) Density of states CaPc (left) and for F₁₆CaPc (right).

To visualize the orbital contributions to the electronic density, we calculate the energy resolved density distribution $n_{\text{LDOS}}(\mathbf{r}) = \int_{E_1}^{E_2} dE N(E, \mathbf{r})$, where $N(E, \mathbf{r})$ is the local density of states. The HOMO and LUMO charge density isosurfaces for CaPc and F₁₆CaPc are shown in Fig. 4, confirming that there is no contribution from the metal atom to these orbitals. This is related to the marked propensity of the alkali metal to loose its valence electrons and to form ionic bonds, transferring the charge to the MPc backbone. Dominating contributions in the case of the HOMO are from carbon atoms whereas orbitals localized on nitrogen and carbon contribute jointly to the LUMO. Therefore this state is more delocalized over the entire inner ring. The symmetry obtained for the HOMO's density indicates that it is an a_{1u} orbital while the LUMO's density concurs with an e_g orbital type, the relative height of their corresponding DOS peak (see Fig. 3) indicates that e_g is a doubly degenerate level.

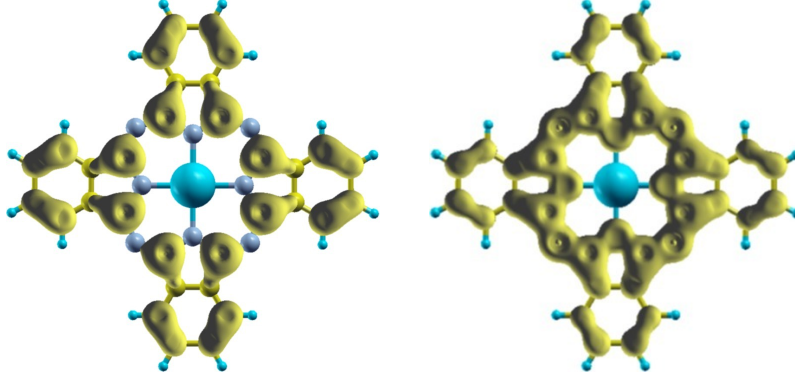


FIG. 4. (Color online) Charge density isosurface for CaPc: HOMO (left), LUMO (right).

The charge density isosurfaces for $F_{16}CaPc$ have almost the same shape as CaPc. In addition, the fluor atoms have clearly visible contributions.

Turning to the 3d-transition metals, the DOS of ScPc and its fluorinated derivative are shown in Fig. 5 and Fig. 6. The states around -1.1 eV are very similar to the HOMO of CaPc. The Sc d majority states show small contributions just below and above the Fermi level due to the mixing of the split d_{xz} and d_{yz} with the e_g ligand orbital which, as mentioned, in CaPc is a LUMO doubly degenerate state. Metal contributions to unoccupied states also appear above 1.2 eV, coming from d_{xy} , d_{xz} , d_{yz} and d_{z^2} . The PBE DOS of ScPc indicates that the d_{xz} contribution to the HOMO increases while it decreases for unoccupied levels appearing at lower energies (down-shift). A wider band gap of 0.3 eV is obtained when PBE is used. Regarding the electronic structure of TiPc (Fig. 7), it can be seen that the metal has more contribution to the HOMO through its d_{xz} and d_{yz} orbitals than in ScPc. PBE predicts a slight HOMO down-shift, a marked peak splitting of d_{xy} and d_{z^2} metallic contributions and a band gap increase of 0.3 eV. These effects concur with the expected reduction of the self-interaction error for the semi-local method.

The electronic structure of $F_{16}ScPc$ (Fig. 6) indicates that states near the Fermi energy are not influenced by fluorination. In contrast, the main difference between TiPc and $F_{16}TiPc$ (Fig. 8) is the level splitting of states with metallic contribution, particularly near the Fermi energy. The change in the admixture of Ti and Pc states modifies the majority DOS profile. Even though fluorination can change the electronic structure, the total magnetic moment is not altered. This is due to the charge redistribution in the molecule, as can be concluded from peak intensity changes of electronic structure states close to E_F . The charge deficiency

on the metal and its magnetization, estimated as the difference between electronic charge densities of opposite spins obtained with the Mulliken population analysis [65], are reported in Tab. II. The table shows that, with the exception of Ti systems, the small amount of charge transferred from the metal to Pc is similar for the fluorinated and not fluorinated compounds. When the tendency of estimated metal magnetizations is compared to that of the total magnetizations, previously shown in Tab. I, it is possible to observe a close interdependence.

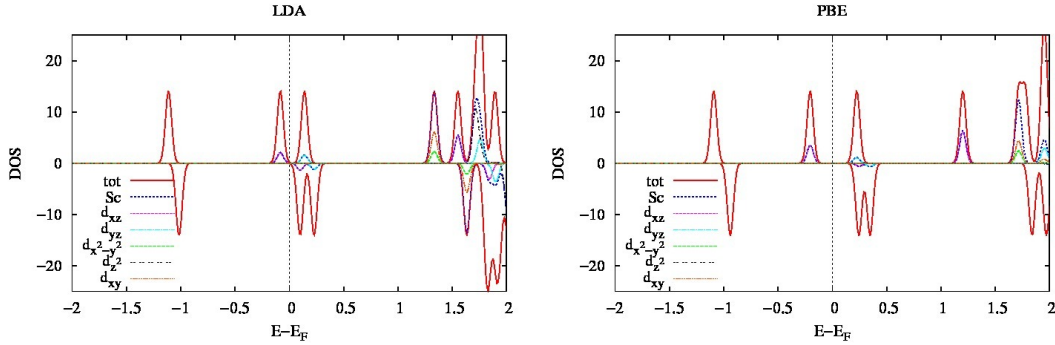


FIG. 5. (Color online) Density of states of ScPc with LDA (left) and PBE (right).

As noted in the second row of Tab. II, the estimated metal magnetization difference between TiPc and F₁₆TiPc is 0.23 μ_B . Along with this increase there is a diminution of 0.11 e of the charge transferred from the metal to the rest of the molecule. This can be understood as a compensation mechanism that explains why both molecules possess equal

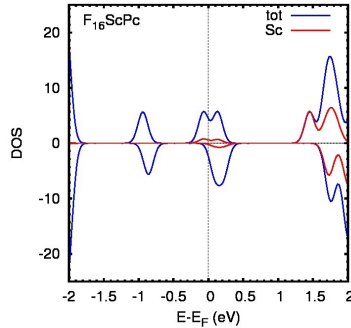


FIG. 6. (Color online) Density of states of F₁₆ScPc with LDA.

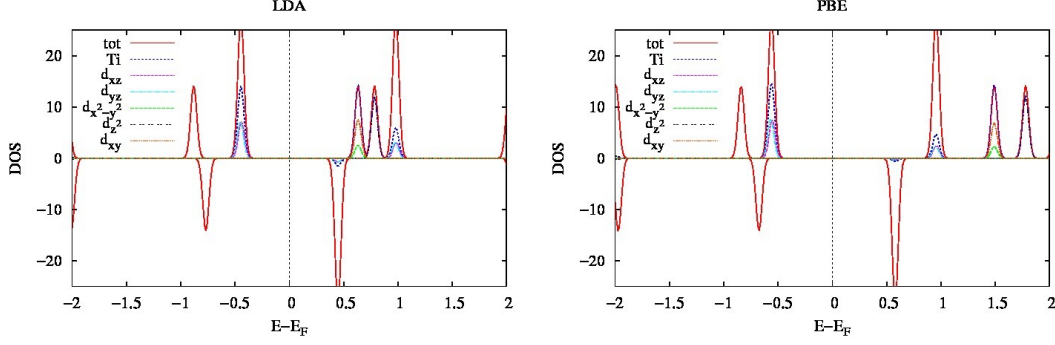


FIG. 7. (Color online) Density of states of TiPc with LDA (left) and PBE (right).

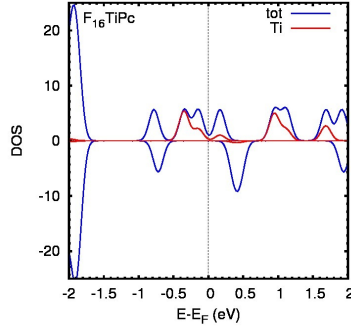


FIG. 8. (Color online) Density of states of F₁₆TiPc with LDA.

total magnetic moments, stressing the ability of these compounds to modify their spin electronic densities by means of metal–ligand charge redistribution.

Considering the LDA majority DOS of VPc, see Fig. 9, we note that new metal orbitals contributing to the occupied states appear between the HOMO and the a_{1u} molecular orbital. They correspond to d_{z^2} , d_{xy} and, to a lesser extend, to $d_{x^2-y^2}$. The degenerate d_{xz} and d_{yz} metal orbitals in the HOMO of TiPc become split in VPc, and they compose its HOMO and LUMO. The band gap is reduced to 0.4 eV. In contrast PBE predicts this gap to be 0.9 eV, displaying a down-shifted HOMO (up-shifted LUMO) with a larger (smaller) metal contribution. Peak heights of d_{z^2} and d_{xy} are similar to the d_{yz} peak at HOMO, hence they are relevant for electron filling along the d -row series. Their energy ordering and particularly

TABLE II. Band gap, metal magnetization and metal charge densities of MPc and F₁₆ MPc

M		Ca	Sc	Ti	V	Cr	Mn	Fe	Co	Ni	Cu	Zn	Ag
Band gap (eV)	MPc	1.5	0.2	0.9	0.4	1.3	0.14	0.4	1.2	1.5	1.1	1.5	0.4
	F ₁₆ MPc	1.3	0.2	0.4	0.5	1.2	0.14	0.4	1.3	1.4	1.4	1.3	0.4
Magnetization (μ_B)	MPc	0.00	0.19	1.47	2.97	4.02	4.78	2.58	1.31	0.00	0.47	0.00	0.38
	F ₁₆ MPc	0.00	0.20	1.70	2.98	4.03	4.83	2.57	1.30	0.00	0.47	0.00	0.38
Charge density (a.u.)	MPc	1.26	0.30	0.28	0.15	0.05	0.48	0.30	0.23	0.14	0.15	0.39	0.25
	F ₁₆ MPc	1.27	0.28	0.17	0.16	0.07	0.48	0.31	0.24	0.15	0.16	0.39	0.26

the position of d_{xy} , indicates that the crystalline field effect is not determinant. In the PBE description the d_{z^2} and d_{xy} metal orbitals appear at lower energies of a_{1u} .

Following along the 3d sequence, the additional electron of Cr causes important changes in the electronic DOS, see Fig. 10. Metal contributions to occupied levels appear below the HOMO. The d_{xz} and d_{yz} orbitals which are split in VPc become degenerate as in TiPc. For the first time within this MPc series the closest orbitals to the Fermi energy show larger energy differences for the majority states than for the minority states. It can be seen that there are no metal contributions to HOMO and LUMO, they principally localize upon the inner ring. HOMO-1 and HOMO-2 (first and second orbital below the HOMO energy) show only a small down-shift with PBE but the band gap remains almost the same.

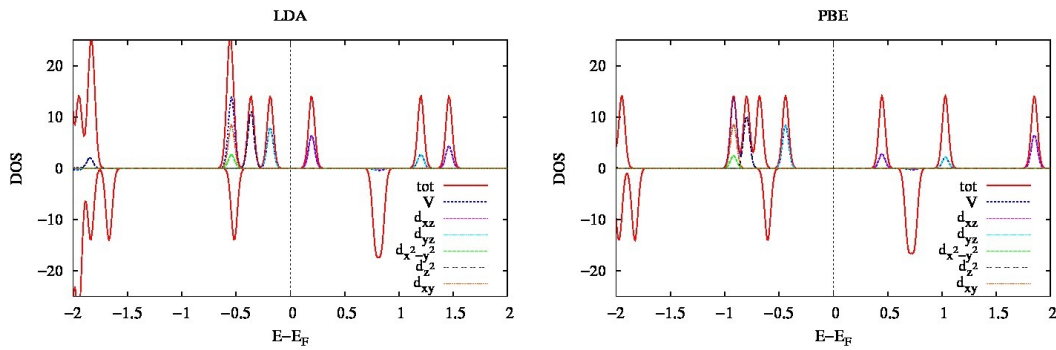


FIG. 9. (Color online) Density of states of VPc with LDA (left) and PBE (right).

The densities of states of MnPc and FePc are shown in Fig. 11 and Fig. 12, respectively. Inside the $-2.0 \dots 2.0$ eV window around the Fermi energy, the only Mn non-negligible

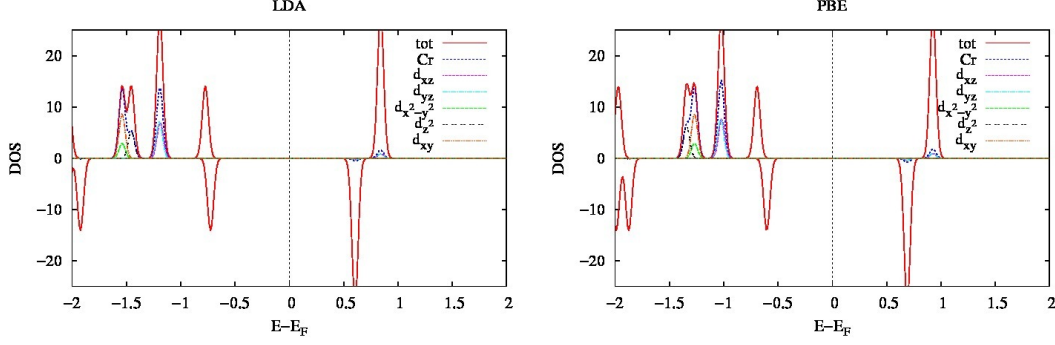


FIG. 10. (Color online) Density of states of CrPc with LDA (left) and PBE (right).

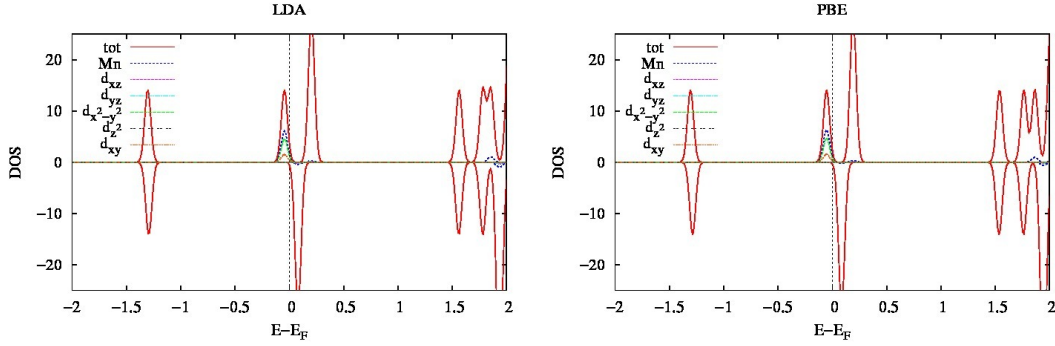


FIG. 11. (Color online) Density of states of MnPc with LDA (left) and PBE (right).

contribution corresponds to the $d_{x^2-y^2}$ (b_{1g}) to the HOMO. Other metal contributions to occupied states, previously seen in VPc and CrPc, appear at energies about 0.5 eV below the HOMO-1 (a_{1u}). The LUMO displays only ligand contribution, then the closest orbitals to the Fermi energy have a metal-ligand character with a narrow band gap of 0.14 eV (within LDA), and 0.18 eV (within PBE). These values are close to the PBE result, 0.21 eV, of Stradi et al. [66] who used different double-zeta (6-31G(d,p)) and triple-zeta basis sets for localized Gaussian-type orbitals (GTO), as well as plane-wave basis sets. Their peak decomposition analysis of DOS indicates that the metal contributes to HOMO and LUMO through d_{yz} and d_{xz} ; this result holds for every method they tested although it significantly reduces for LUMO with PBE0 and HSE06. Different functionals (PBE, B3LYP, PBEh and M06) have

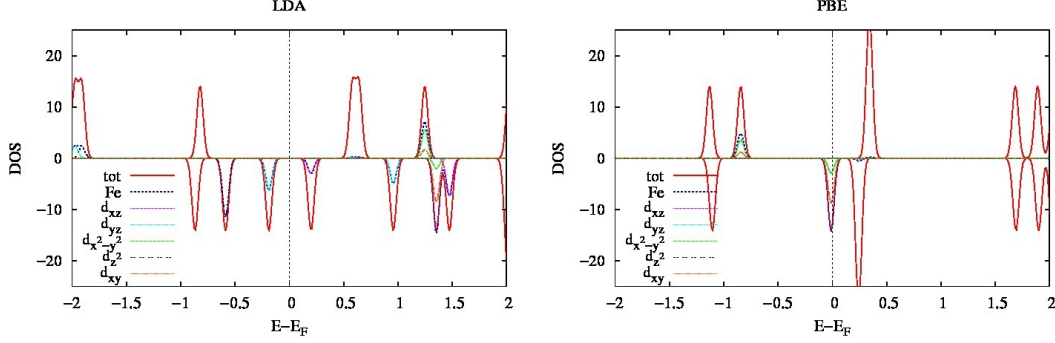


FIG. 12. (Color online) Density of states of FePc with LDA (left) and PBE (right).

predicted either of two configurations if symmetry is enforced, $a_{1g} \downarrow(\text{HOMO}) e_g \downarrow(\text{LUMO})$ and $b_{2g} \downarrow(\text{HOMO}) e_g \downarrow(\text{LUMO})$ [58]. On the other hand, when symmetry restrictions are not used either of two configurations are obtained, $e_g \downarrow(\text{HOMO}) e_g \uparrow(\text{LUMO})$ and $e_g \downarrow(\text{HOMO}) e_g \downarrow(\text{LUMO})$, as reported in the same work. Qualitatively, our result agrees with those configurations with a metal (ligand) contribution to the HOMO (LUMO) state. Both theoretical works point out that the calculated eigenvalue spectra of isolated MnPc appears compressed (into a smaller energy window) by about 20 % with respect to the reported data of the UPS experiment for thin and thick films deposited on metal surfaces. A more direct comparison is not possible because data for the gas phase are not available, and our calculations are basically for isolated molecules.

In FePc, the addition of one electron initiates the second half of the d -shell, where now the atomic orbitals can have two electrons, bringing about more possibilities to accommodate electrons and increasing the electron correlation due to the electron pairing. The HOMO and LUMO can be identified as e_g orbitals with d_{yz} and d_{xz} metal contributions, respectively, when using LDA, and $d_{x^2-y^2}$ metal orbital and e_g with PBE. Regarding the metal (ligand) character of HOMO (LUMO), our PBE and LDA result concurs with recent calculations [60, 67–69] but deviates from another prediction [58]. Furthermore, several theoretical works devoted to the interpretation of experimental results differ in the assessment of metal or ligand character of HOMO and LUMO. The analysis of electron energy-loss spectral data for FePc films [70] strongly suggests that partially occupied states e_g , with d_{yz} and d_{yz} metal contributions, lie in between a_{1u} and e_g ligand states, manifesting metal participation for

HOMO with an energy difference to LUMO (e_g orbital on the ligand) of 0.45 eV, very close to our LDA band gap, 0.4 eV, and PBE, 0.5 eV, estimates. The occurrence of metal orbitals close to the Fermi level, particularly for HOMO, has also been concluded from the analysis and interpretation of photoemission and X-ray absorption spectroscopy measurements of FePc on Ag(111) [71]. The metal–ligand character obtained with LDA for HOMO–LUMO is used to describe the charge transfer between FePc and Au(111) [72] by means of the LDA+U method. Analogously the GGA+U method is employed to reproduce charge reorganization of FePc adsorbed on Ag(100) deduced from STM spectroscopy [69]. Apart from the +U correction our results differ in a qualitative manner because we find d_{z^2} states close the Fermi level but not d_{xy} , instead we get $d_{x^2-y^2}$. This may be due to a larger degree of metal–ligand hybridization for d_{xy} . In contrast a ligand–ligand character is suggested to account for photoelectron spectroscopy experiments which help to determine U_{eff} within the GGA+U correction [67]. Nevertheless, recent total-energy density functional calculations together with density-matrix constraints indicate that isolated and columnar stacking FePc molecules (α -FePc) ground states have a substantial d metal orbital contribution to HOMO [68].

Figure 13 displays the density of states for CoPc. The LDA band gap, 1.2 eV, is larger than the previously reported result, 1.0 eV [8], using LDA and GGA+vdW. The band gap obtained with GGA, 1.45 eV, is the same as the one predicted for a CoPc monolayer [40] by the full-potential linearized augmented plane wave (FLAPW) method, and very close to the GGA+U result of 1.4 eV [69], but smaller than the calculated value of 1.96 eV [35] using the Vosko-Wilk-Nusair (VWN) potential [42] including exchange and correlation gradient corrections. In the majority component, LDA and PBE indicate that HOMO and LUMO are distributed over the Pc atoms. From the charge density isosurface (Fig. 14) of the occupied Co states from -2 eV to E_F , we see that the contribution to the majority density principally derives from Co and N states while carbon atoms contribute to minority states. In regard to the LDA DOS, we find that the metal-localized occupied d_{z^2} orbital down-shifts in the GGA description, on the contrary the LUMO, d_{xy} , up-shifts and the $2e_g$ orbital becomes LUMO. The ligand (a_{1g}) – ligand ($2e_g$) character of HOMO – LUMO, differs from the metal (d_{z^2}) – ligand [40], ligand – metal [61], ligand ($1e_g$) – ligand ($2e_g$) [35] character of other works, but agrees with recent theoretical results [69] in the gas phase, carried out to account for STM experimental observations.

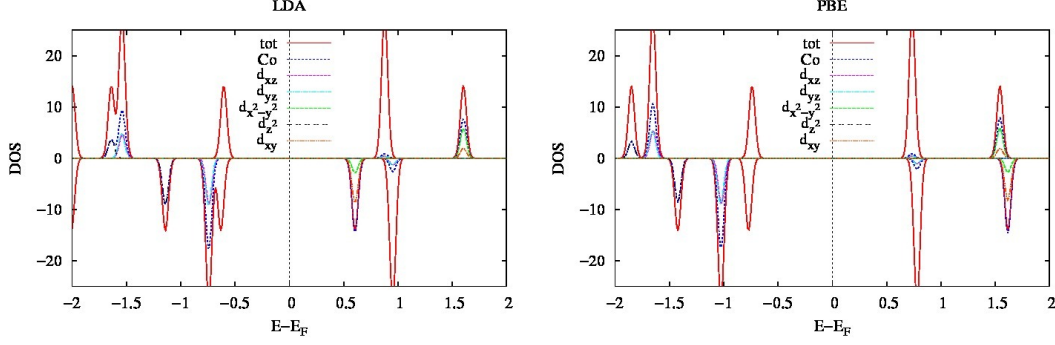


FIG. 13. (Color online) Density of states of CoPc with LDA (left) and PBE (right).

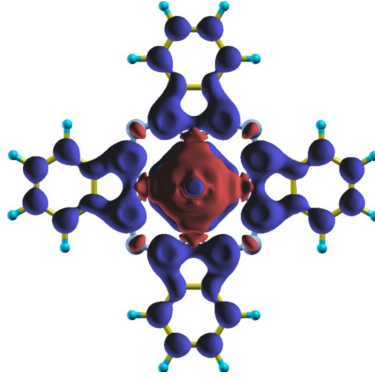


FIG. 14. (Color online) Charge density isosurface for occupied states, red minority-spin and blue majority-spin electron density.

From the NiPc DOS functions shown in Fig. 15, it can be noted that there is no difference between majority and minority spin densities. The electron pairing that occurs in this close-shell system causes equal positions and the same orbital order for both spins. Metal orbitals forming occupied orbitals are found below the HOMO, while at the same time there are only very small Ni $d_{xz,yz}$ contributions to the LUMO orbitals giving a ligand – ligand character to HOMO – LUMO with the same band gap of 1.5 eV for both spins. This value is smaller than the one obtained with the Hartree-Fock (HF) method, 2.41 eV [38], but larger than the LDA prediction, 0.7 eV, for the monolayer and crystal monoclinic phase in the same work. Our band gap is very close to the estimation with the VWN potential of 1.47 eV [35], but that study also reported that the LUMO corresponds to a b_{1g} orbital, like a later PBE evaluation [2]. Regarding the band gap value and LUMO+1's identity, our result

agrees with more recent GGA+U [69] and Spectroscopy-Oriented Configuration Interaction (SORCI) calculations [60].

The DOS functions of CuPc (Fig. 16) indicates that splitting between $b_{1g} \uparrow$ and $b_{1g} \downarrow$ increases when the PBE functional is used, making the a_{1u} orbital the HOMO and leaving the $b_{1g} \downarrow$ as LUMO. This up- and down-shift of occupied and unoccupied orbitals, respectively, is consistent with the expected reduction of the self-interaction error for localized levels. The ordering agrees with recent GGA+U calculation including the 1.4 eV band gap [69], and differs from SORCI results [60], and previous VWN predictions [35].

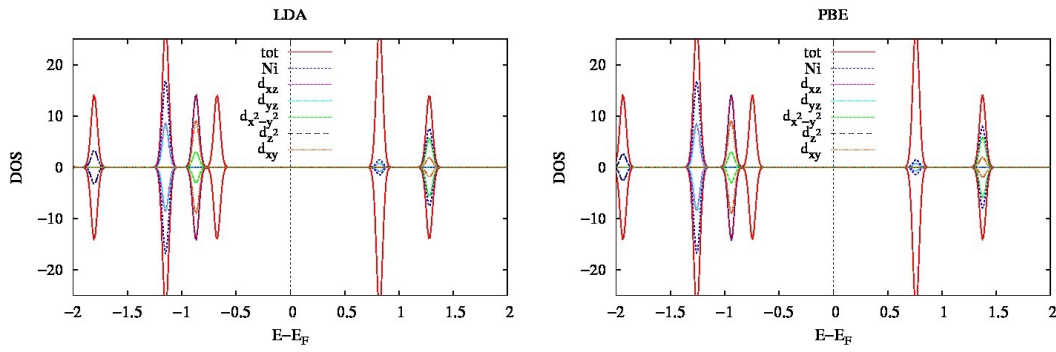


FIG. 15. (Color online) Density of states of NiPc with LDA (left) and PBE (right).

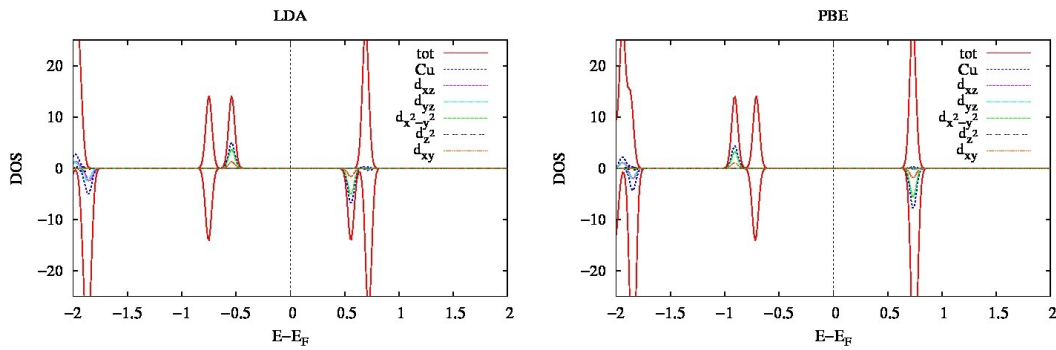


FIG. 16. (Color online) Density of states of CuPc with LDA (left) and PBE (right).

The last two structures we discuss are ZnPc and AgPc. For ZnPc, the Zn metal states overlap with C and N states at 1.2 eV for the majority and minority states, see Fig. 17. The

C and N contributions to the states are observed above -1.2 eV, specifically at -0.75 eV for C orbitals and at 0.75 eV for C and N orbitals. The band gap is 1.5 eV, similar to the CaPc molecule, but smaller than a previously reported value [31]. For AgPc, the Ag states mix with the N and C states at -0.1 eV for the majority states, and at 0.7 eV for the minority states. The pure C states prevail at -1.3 eV, C and N states at 0.2 eV and above 1.4 eV; thus it is difficult to decide whether AgPc becomes metallic or semiconducting, see Fig. 18.

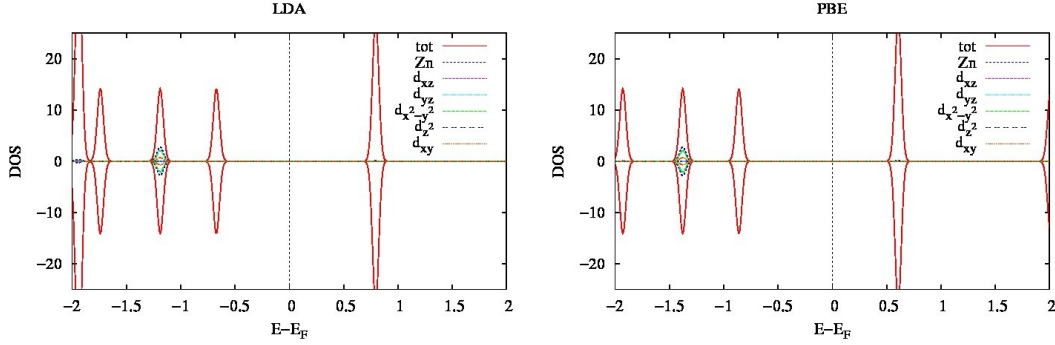


FIG. 17. (Color online) Density of states of ZnPc with LDA (left) and PBE (right).

The band gaps for F_{16} MPc and for MPc are given in Tab. II. The gap of each F_{16} MPc is less than or equal to the gap of the corresponding MPc, which can be correlated to the fact that fluor is more electronegative, thus the electronic density in the central region of the molecule is more strongly attracted to the surrounding shell.

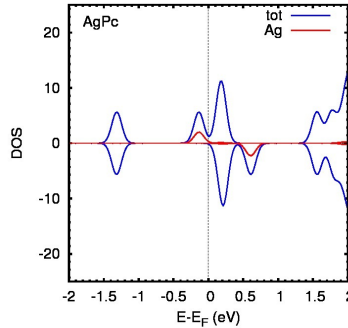


FIG. 18. (Color online) DOS of AgPc.

IV. VIBRATIONAL PROPERTIES OF METAL PHTHALOCYANINES

The comparison of the calculated frequencies with experimental data of ZnPc indicates a semi-quantitative agreement for the main characteristics of Raman and infrared (IR) spectra (Tab. III). The experimental Raman spectra presented in Fig. 7 from the work of Tackley et al. [30] displays three bands which are more intense than the rest; our results coincide with their positions within 10 cm^{-1} with the exception of the most intense band at 1505 cm^{-1} .

TABLE III. Frequencies (cm^{-1}) of relevant vibrational modes of ZnPc, and comparison with CuPc

	ZnPc			CuPc
	Experimental ^a	Calculated ^a	Calculated ^b	Calculated ^c
Raman	1505	1517	1566	1609
	1447	1438	1448 ^d	1491
	1340	1362	1347 ^d	1395
	1144	1004	-	1351
		1134	-	1169
		1278	-	1035
	747	735	737	763
IR	727	703	706	730
	752	741	-	769
	780	760	-	786

^aFrom reference [30], ^bOur CA/DZP calculation

^cOur B3LYP/6-31G** calculation

^dSorted only by numerical value. See text for explanation.

Our calculated frequencies of 1448 cm^{-1} and 1347 cm^{-1} are close to the experimental bands at 1447 cm^{-1} and 1340 cm^{-1} , however, their displacement eigenvectors have more

similarities with those found in previously reported vibrational modes at 1438 cm^{-1} and 1278 cm^{-1} , respectively (see supplementary information of [30]). The IR and Raman nature of each vibrational mode considered here is compared to and confirmed through the displacement vector analysis of the calculated results for CuPc, also shown in Tab. III. The match between each vibrational mode type (IR) between ZnPc and CuPc give us the confidence to extrapolate these results to the rest of the MPc studied here.

TABLE IV. Frequencies (cm^{-1}) of relevant vibrational modes for MPc

Mode description	Sc	Ti	V	Cr	Mn	Fe	Co	Ni	Cu	Zn
Metal out-of-plane	85	122	108	144	54	110	168	184	148	110
Asymm. breathing	–	193	205	201	171	175	191	197	174	159
Symm. breathing	–	–	262	262	229	–	260	255	259	264
Ip ^a N–M–N bending	194	203	209	210	202	208	243	243	220	218
Op ^b asymm. M–N ₄ bending	–	279	–	275	–	243	314	–	250	223
Op ^b symm. M–N ₄ bending	342	351	381	345	–	361	372	394	331	226

^a Ip = in-plane, ^b Op = out-of-plane

TABLE V. Frequencies (cm^{-1}) of relevant vibrational modes for MPc

Mode description	Sc	Ti	V	Cr	Mn	Fe	Co	Ni	Cu	Zn
M–N ₂ stretching-bending	326	341	352	357	312	309	389	345	301	241
M–N ₂ stretching-bending	329	342	358	363	316	363	401	351	302	245
M–N ₄ asymm. stretching	544	545	542	546	537	511	546	542	539	533
M–N ₄ symm. stretching	576	574	572	576	569	575	581	578	577	576
M–N ₄ asymm. stretching	1325	1183	1205	1357	1303	1342	1359	1362	1351	1347
M–N ₄ symm. stretching	1366	1337	1387	1401	1348	1375	1407	1407	1403	1409

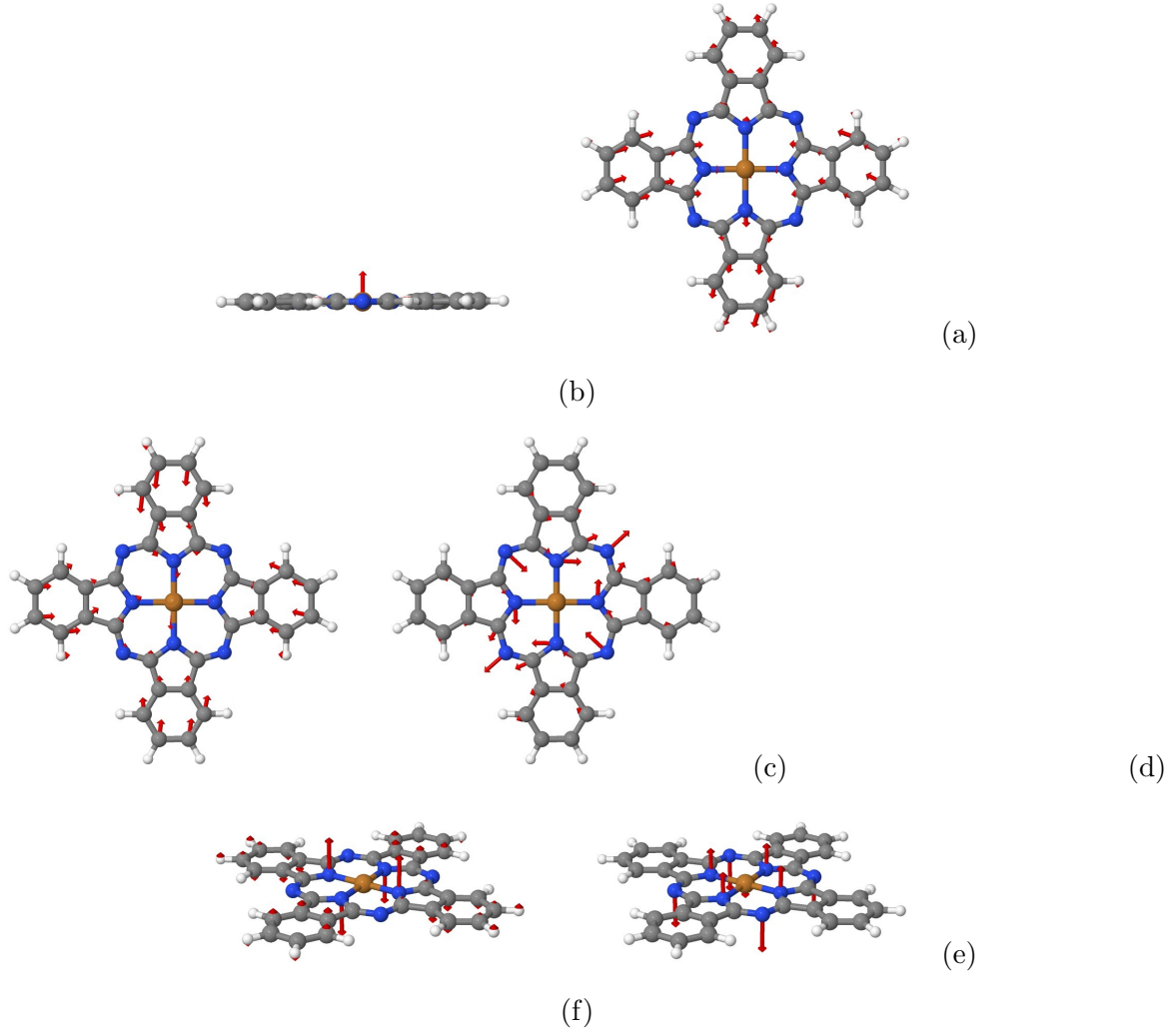


FIG. 19. (Color online) Selected vibrational modes of CuPc also observed in other MPc, and described as metal out-of-plane displacement (a), asymmetric (b) and symmetric (c) breathing, in-plane N–M–N bending (d), out-of-plane asymmetric (e) and symmetric (f) M–N₄ bending.

Tables IV and V show calculated frequencies of the MPc complexes for relevant vibrational modes such as breathing, and for those which involve atomic displacement near the metal. Displacement vectors for such modes are schematically presented in Figs. 19 and 20. As expected, symmetric vibrational modes are found at higher frequencies than asymmetric modes, but their frequency shift, when the metal center is varied, depends on the particular mode. Symmetric and asymmetric breathing movements of the entire molecule show similar

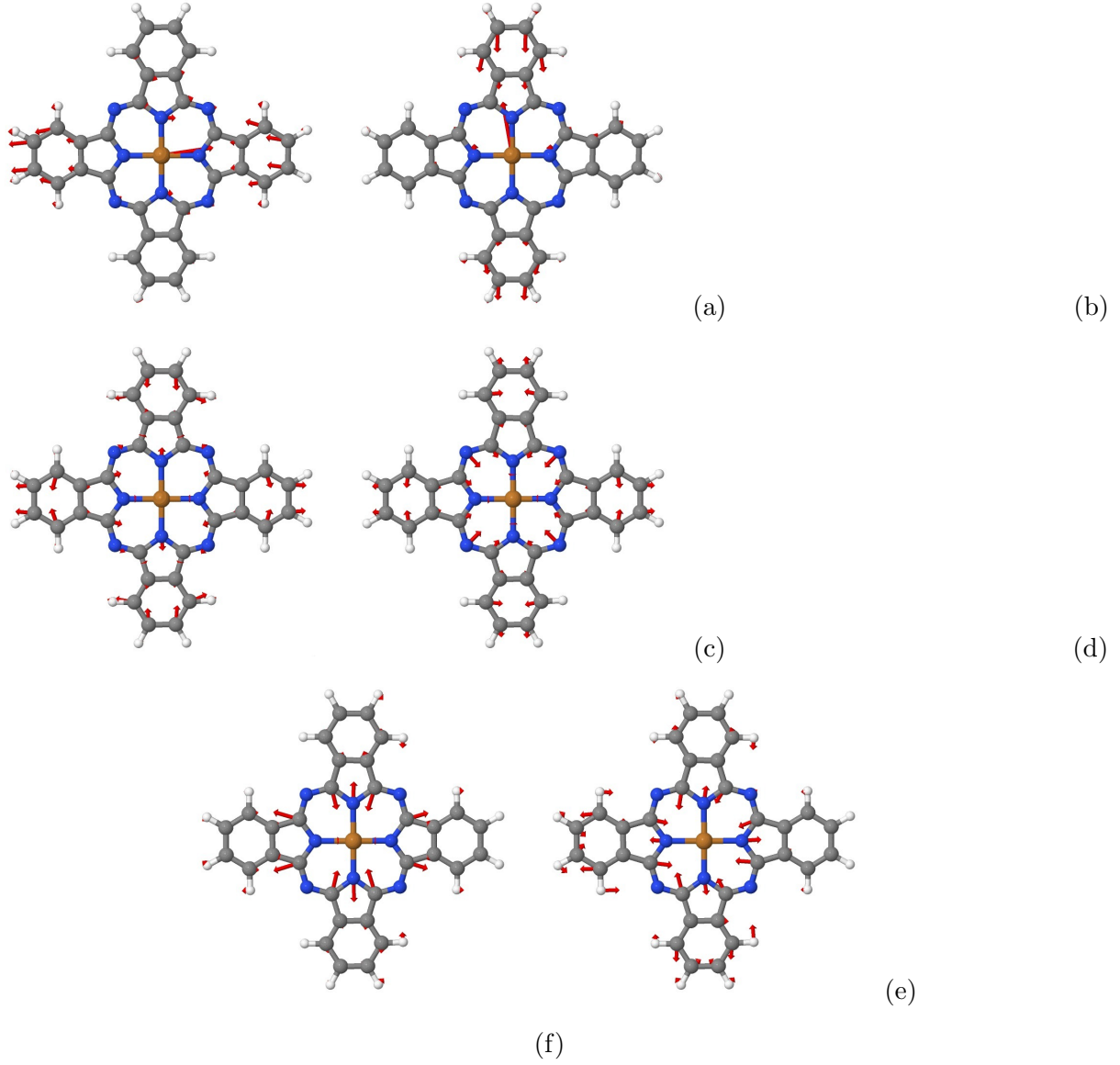


FIG. 20. (Color online) Selected vibrational modes of CuPc, also observed in other MPc. M–N₂ stretching-bending, (a) and (b); M–N₄ asymmetric ((c), (e)) and symmetric ((d), (f)) stretching.

magnitudes of frequency shifts, the main difference being that frequencies of asymmetric breathing modes increase when going from Zn to Co, while the opposite tendency is found for the symmetric modes (see Fig. 21). This behavior may be explained by the release of stress around the metal inside the ring when it opens simultaneously in all directions.

In the case of the M–N₄ stretching modes, it is apparent from Fig. 21 that there is

a consistent increase from Zn to Co or Ni for the asymmetric type. The high-frequency ($> 1180 \text{ cm}^{-1}$) modes of M-N₄ stretching have larger shifts. Their frequencies decrease from Fe to Co, then they increase again for Cr. These variations are not present for low frequency ($< 600 \text{ cm}^{-1}$) M-N₄ stretching modes: this can be understood on the basis of their displacement vectors (Fig. 20), which indicate significant deformations of benzene rings and smaller displacements on atoms close to the metal. Vibrational modes which involve atomic displacements near the metal show larger shifts. For bendings the magnitude of the shifts can be tens of cm^{-1} . There is a frequency increase from Zn to Co, then a decrease for Fe, and an increase again for Cr. This is found for out-of-plane M-N₄ bending, and for M-N₂ stretching-bending modes.

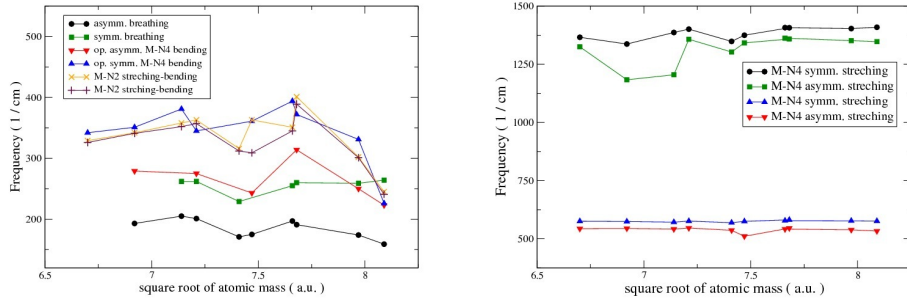


FIG. 21. (Color online) Frequencies of selected vibrational modes of MPc

In Tab. VI we compare our frequency values and the nature of vibrational modes of CuPc with those reported in [73] for the fluorinated system FCuPc, particularly for those which were found to have a larger contribution to the energy transfer process. Frequency values for CuPc become similar to results for FCuPc when the vibrational modes involve a small number of atoms, and when the atomic displacements are mainly from atoms closer to the metal. The above trends are also obtained with PBE.

TABLE VI. Comparison of frequencies (cm^{-1}) of relevant vibrational modes of CuPc and FCuPc

FCuPc ^a	175	983	1445	1570
CuPc ^b	201	1158	1401	1561

^aFrom reference [73]

^bOur CA/DZP calculation

V. SUMMARY

The magnetic and electronic properties of metal phthalocyanines (MPc) and fluorinated metal phthalocyanines (F_{16}MPc) have been studied by spin density functional theory for the first row-transition metals. CaPc and AgPc were also considered for comparison. A planar geometry with the metal lying inside the inner ring was obtained for all MPc except for the cases $M = \text{Ca}$ and Sc , which are displaced from the plane by 1.12 \AA and 0.24 \AA , respectively, in direct relation with their atomic sizes. The analysis of electronic states shows that the total magnetic moment is caused mainly by the electron density localized on the metal and its nearby atoms. Furthermore, when the hydrogen atoms are replaced by fluor atoms the magnetic moments do not change. The same behavior is found for the band gap values. The M-N bond lengths of F_{16}MPc are slightly larger than the corresponding ones of MPc.

On the other hand, the analysis of the density of states (DOS) indicates a substantial change in the number, position, width and height of the DOS peaks in F_{16}MPc in comparison to MPc. The fact that the total magnetic moment values do not change can be explained by the charge density redistribution between the metal and its nitrogen and carbon neighbors. This rearrangement suggests a high flexibility of the electronic distribution which may account for the apparent independence of the MPc properties on the metal, also pointed out in previous works [74]. However, the DOS profiles obtained along the studied d -row series indicate different mixing between metal and ligand orbitals, and corresponding energy shifts.

The crystal field approximation cannot account for the orbital mixing occurring in these compounds. The ligand orbitals a_{1u} and e_g have the propensity to appear near the Fermi energy and they can become HOMO or LUMO when the electronic repulsion shifts localized states on the metal or when electron pairing on the metal compensates repulsion between

levels for both spins as in NiPc and ZnPc. Near the middle of the studied d series, repulsion among unpaired electron densities causes different DFT functionals to disagree with respect to the electronic structure. However, we have found that in general, LDA results are valuable for the qualitative assessment of the metallic or ligand character of the HOMO and the LUMO. Comparison with PBE results is useful to determine which localized metal orbitals are more strongly affected by the self-interaction error. The observed tendencies may be extrapolated to understand and predict the device performance of particular MPc employed in organic solar cells in which the exciton diffusion is affected by the energetical ordering of the orbitals [60].

The band gap shows a steep drop from CaPc to ScPc, i.e., when the d shell is initiated. The largest value found in the d^2 - d^4 interval is for CrPc, and another important decrease is predicted for MnPc. The semiconducting character is recovered for the d^7 - d^{10} series with low spin configuration. The crucial effect of the central metal in the electronic properties of MPc helps to explain recent theoretical results about the energetics of their adsorption on an Au(111) surface [61], as well as the increasing impact of the $3d$ states along the ZnPc–MnPc series as determined by energy-loss and photoemission spectroscopy [75]. Ongoing research regarding electron transport on these MPc is being carried out in our group.

Based on the vibrational mode analysis, we find that, in general, frequencies increase when going from Zn to Fe if they correspond to asymmetric modes. There is an increment from either Mn or Fe to Cr. The series V, Ti, and Sc shows a more irregular behavior. However, there is a consistent frequency decrease from V to Sc for vibrational modes which do not include breathing or metal out-of-plane movement. The vibrational frequencies change a few tens of cm^{-1} when the metal in the central position is varied. This is an order of magnitude larger than the shifts provoked by molecular adsorption [76].

Acknowledgement

We thank P. Schwab for helpful discussions. Financial support by the Deutsche Forschungsgemeinschaft (through TRR 80), PPPROALMEX-DAAD-Conacyt binational support, Project SEP-CONACYT 152153, CNS-IPICyT, Mexico and TACC-Texas supercomputer center for providing computational resources. O. I. A.-F. thanks Camilo Garcia for valuable discussions and CONACyT for a postdoctoral fellowship. AHR acknowledges support from

the Marie-Curie Intra-European Fellowship program.

- [1] J. Van den Brink and A. F. Morpurgo, *Nature* **450**, 117 (2007).
- [2] N. Marom and L. Kronik, *Appl. Phys. A* **95**, 159 (2009).
- [3] S. A. V. Slyke, C. H. Chen and C. W. Tang, *Appl. Phys. Lett.* **69**, 2160 (1996).
- [4] P. Peumans and S. R. Forrest, *Appl. Phys. Lett.* **79**, 126 (2001).
- [5] P. C. Kao, S. Y. Chu, Z. X. You, S. J. Liou and C. A. Chuang, *Thin Solid Films* **498**, 249 (2006).
- [6] Z. N. Bao, A. J. Lovinger and A. Dodabalapur, *Appl. Phys. Lett.* **69**, 3066 (1996).
- [7] R. W. I. de Boer, A. F. Stassen, M. F. Craciun, C. L. Mulder, A. Molinari, S. Rogge and A. F. Morpurgo, *Appl. Phys. Lett.* **86**, 262109 (2005).
- [8] X. Chen and M. Alouani, *Phys. Chem. B* **82**, 094443 (2010).
- [9] H. Huang, W. Chen and A. T. S. Wee, *J. Phys. Chem. C* **112**, 14913 (2008).
- [10] T. Wang, D. Ebeling, J. Yang, C. Du, L. F. Chi, H. Fuchs and D. Yan, *J. Phys. Chem. B* **113**, 2333 (2009).
- [11] D. G. de Oteyza, E. Barrena, J. O. Osso, S. Sellner and H. Dosch, *J. Am. Chem. Soc.* **128**, 15002 (2006).
- [12] D. G. de Oteyza, E. Barrena, Y. Zhang, T. N. Krauss, A. Turak, A. Vorobiev and H. Dosch, *J. Phys. Chem. C* **113**, 4234 (2009).
- [13] L. Scudiero, K. W. Hipps and D. E. Barlow, *J. Phys. Chem. B* **107**, 2903 (2003).
- [14] K. W. Hipps, L. Scudiero, D. E. Barlow and M. P. Cooke, *J. Am. Chem. Soc.* **124**, 2126 (2002).
- [15] C. J. Drury, C. M. J. Mutsaers, C. M. Hart, M. Matters and D. M. de Leeuw, *Appl. Phys. Lett.* **73**, 108 (1998).
- [16] Y. Watanabe and K. Kudo, *Appl. Phys. Lett.* **87**, 223505 (1995).
- [17] R. Wisniewski, *Nature* **394**, 225 (1998).
- [18] B. Crone, A. Dodabalapur, A. Gelperin, L. Torsi, H. E. Katz, A. J. Lovinger and Z. Bao, *Appl. Phys. Lett.* **78**, 2229 (2001).
- [19] B. K. Crone, A. Dodabalapur, R. Sarpeshkar, A. Gelperin, H. E. Katz and Z. Bao, *J. Appl. Phys.* **91**, 10140 (2001).

- [20] A. Dodabalapur, Z. Bao, A. Makhija, J. G. Laquindanum, V. R. Raju, Y. Feng, H. E. Katz and J. Rogers, *Appl. Phys. Lett.* **73**, 142 (1998).
- [21] C. J. Brown, *J. Chem. Soc. A* , 2488 (1968).
- [22] J. F. Kirner, W. Dow, and W. R. Scheidt, *Inorg. Chem.* **15**, 1658 (1976).
- [23] W. R. Scheidt and W. Dow, *J. Am. Chem. Soc.* **99**, 1101 (1977).
- [24] F. Evangelista, V. Carravetta, G. Stefani, B. Jansik, M. Alagia, S. Stranges and A. Ruocco, *J. Chem. Phys.* **126**, 124709 (2007).
- [25] Xiao and P. A. Dowben, *J. Mater. Chem.* **19**, 2172 (2009).
- [26] K. W. Hipps, X. Lu, X. D. Wang and U. Mazur, *J. Phys. Chem.* **100**, 11207 (1996).
- [27] P. H. Lippel, R. J. Wilson, M. D. Miller, C. Woll and S. Chiang, *Phys. Rev. Lett.* **62**, 171 (1989).
- [28] M. Filibian, P. Carretta, T. Miyake, Y. Taguchi and Y. Iwasa, *Phys. Rev. B* **75**, 085107 (2007).
- [29] T. Schwieger, H. Peisert, M. S. Golden, M. Knupfer and J. Fink, *Phys. Rev. B* **66**, 155207 (2002).
- [30] D. R. Tackley, G. Dent and W. E. Smith, *Phys. Chem. Chem. Phys.* **2**, 3949 (2000).
- [31] K. A. Nguyen and R. Pachter, *J. Chem. Phys.* **114**, 10757 (2001).
- [32] N. Papageorgiou, Y. Ferro, E. Salomon, A. Allouche, L. G. J. M. L  ayet and G. L. Lay, *Phys. Rev. B* **68**, 235105 (2003).
- [33] A. Rosa, G. Ricciardi, O. Gritsenko and E. J. Baerends, *Structure and Bonding* **112**, 49 (2004).
- [34] J. P. Gauyacq, F. D. Novaes and N. Lorente, *Phys. Rev. B* **81**, 165423 (2010).
- [35] M. S. Liao and S. Scheiner, *J. Chem. Phys.* **114**, 9780 (2001).
- [36] L. Lozzi, S. Santucci, S. L. Rosa, B. Delley and S. Picozzi, *J. Chem. Phys.* **121**, 1883 (2004).
- [37] B. Bialek, I. G. Kim and J. I. Lee, *Synthetic Metals* **129**, 151 (2002).
- [38] B. Bialek, I. G. Kim and J. I. Lee, *Thin Solid Films* **436**, 107 (2003).
- [39] B. Bialek, I. G. Kim and J. I. Lee, *Surface Science* **526**, 367 (2003).
- [40] B. Bialek, I. G. Kim and J. I. Lee, *Thin Solid Films* **513**, 110 (2006).
- [41] N. Marom, O. Hod, G. E. Scuseria and L. Kronik, *J. Chem. Phys.* **128**, 164107 (2008).
- [42] S. H. Vosko, L. Wilk and M. Nusair, *Can. J. Phys.* **58**, 1200 (1980).
- [43] A. D. Becke, *Phys. Rev. A* **38**, 3098 (1988).

- [44] A. D. Becke, *Phys. Rev. B* **33**, 8822 (1986).
- [45] P. J. Stephens, F. J. Devlin, C. F. Chabalowski and M. J. Frisch, *J. Phys. Chem.* **98**, 11623 (1994).
- [46] J. P. Perdew, K. Burke and M. Ernzerhof, *Phys. Rev. Lett.* **77**, 3865 (1996).
- [47] J. P. Perdew, A. Ruzsinszky, J. Tao, V. N. Staroverov, G. E. Scuseria and G. I. Csonka, *J. Chem. Phys.* **123**, 062201 (2005).
- [48] J. Heyd, G. E. Scuseria and M. Ernzerhof, *J. Chem. Phys.* **118**, 8207 (2003).
- [49] S. Bhattacharjee, B. Brena, R. Banerjee, H. Wende, O. Eriksson and B. Sanyal, *Chem. Phys.* **377**, 96 (2010).
- [50] J. M. Soler, E. Artacho, J. D. Gale, A. García, J. Junquera, P. Ordejón and D. Sánchez-Portal, *J. Phys.: Condens. Matter* **14**, 2745 (2002).
- [51] J. L. Kahl, L. R. Faulkner, K. Dwarakanath and H. Tachikawa, *J. Am. Chem. Soc.* **108**, 5434 (1986).
- [52] C. Clarisse, M. T. Riou, M. Gauneau and M. Le Contellec, *Electron. Lett.* **24**, 674 (1988).
- [53] L. Li, Q. Tang, H. Li, W. Hu, X. Yang, Z. Shuai, Y. Liu and D. Zhu, *Pure Appl. Chem.* **80**, 2231 (2008).
- [54] H.-Z. Chen, C. Pan and M. Wang, *Nanostructured Material* **11**, 523 (1999).
- [55] H. Tada, H. Touda, M. Takada and K. Matsushige, *Appl. Phys. Lett.* **76**, 873 (2000).
- [56] D. E. Barlow and K. W. Hipps, *J. Phys. Chem. B* **104**, 5993 (2000).
- [57] Y. L. Pan, Y. J. Wu, L. B. Chen, Y. Y. Zhao, Y. H. Shen, F. M. Li, S. Y. Shen and D. H. Huang, *Appl. Phys. A* **66**, 569 (1998).
- [58] N. Marom and L. Kronik, *Appl. Phys. A* **95**, 165 (2009).
- [59] X. Shen, L. Sun, Z. Yi, E. Benassi, R. Zhang, Z. Shen, S. Sanvito and S. Hou, *Phys. Chem. Chem. Phys.* **12**, 10805 (2010).
- [60] I. Bruder, J. Schöneboom, R. Dinnebier, A. Ojala, S. Schäfer, R. Sens, P. Erk and J. Weis, *Org. Electron.* **11**, 377 (2010).
- [61] Y. Y. Zhang, S. X. Du and H. J. Gao, *Phys. Rev. B* **84**, 125446 (2011).
- [62] G. A. Williams, B. N. Figgis, R. Mason, S. A. Mason and P. E. Fielding, *J. Chem. Soc. Dalton Trans.* , 1688 (1980).
- [63] J. M. Robertson and I. Woodward, *J. Chem. Soc.* , 219 (1937).
- [64] C. Ruan, V. Mastryukov and M. Fink, *J. Chem. Phys.* **111**, 3035 (1999).

- [65] R. S. Mulliken, *J. Chem. Phys.* **36**, 3428 (1962).
- [66] D. Stradi, C. Díaz, F. Martín and M. Alcamí, *Theor. Chem. Acc.* **128**, 497 (2011).
- [67] B. Brena, C. Puglia, M. de Simone, M. Coreno, K. Tarafder, V. Feyer, R. Banerjee, E. Göthelid, B. Sanyal, P. M. Oppeneer and O. Eriksson, *J. Chem. Phys.* **134**, 074312 (2012).
- [68] K. Nakamura, Y. Kitaoka, T. Akiyama, T. Ito, M. Weinert and A. J. Freeman, *Phys. Rev. B* **85**, 235129 (2012).
- [69] A. Mugarza, R. Robles, C. Krull, R. Korytár, N. Lorente and P. Gambardella, *Phys. Rev. B* **85**, 155437 (2012).
- [70] F. Roth, A. König, R. Kraus, M. Grobosch, T. Kroll and M. Knupfer, *Eur. Phys. J. B* **74**, 339 (2010).
- [71] F. Petraki, H. Peisert, U. Aygöl, F. Latteyer, J. Uihlein, A. Vollmer and T. Chassé, *J. Phys. Chem. C* **116**, 11110 (2012).
- [72] E. Minamitani, D. Matsunaka, N. Tsukahara, N. Takagi, M. Kawai and Y. Kim, *e-J. Surf. Sci. Nanotech.* **10**, 38 (2012).
- [73] F. C. Wu, H. L. Cheng, C. H. Yen, J. W. Lin, S. J. Liu, W. Y. Chou and F. C. Tang, *Phys. Chem. Chem. Phys.* **12**, 2089 (2010).
- [74] A. F. Takács, F. Witt, S. Schmaus, T. Balashov, M. Bowen, E. Beaurepaire and W. Wulfhekel, *Phys. Rev. B* **78**, 233404 (2008).
- [75] M. Grobosch, C. Schmidt, R. Kraus and M. Knupfer, *Org. Electron.* **11**, 1483 (2010).
- [76] G. S. S. Saini, S. D. Dogra, K. Sharma, S. Singh, S. K. Tripathi, V. Sathe and R. Singh, *Vib. Spectrosc.* **57**, 61 (2011).